Sea Surface Velocity Vector Retrieval Using Dual-Beam Interferometry: First Demonstration

Jakov V. Toporkov, *Senior Member, IEEE*, Dragana Perkovic, *Student Member, IEEE*, Gordon Farquharson, *Member, IEEE*, Mark A. Sletten, *Senior Member, IEEE*, and Stephen J. Frasier, *Senior Member, IEEE*

***Abstract*—The dual-beam interferometer consists of two interferometric synthetic aperture radars (InSARs), one squinted at 20° forward of broadside, and the other 20° aft, to allow measurement of vector surface velocity with only a single aircraft pass. Estimates of surface velocity vectors in the coastal region during high tidal flow are presented. The data were gathered over the barrier islands west of Fort Myers, FL, as part of a March 2004 deployment. Whereas no detailed bathymetry data were available, high-quality aerial photography appears to be a useful tool in inferring bottom topography and possible current obstructions. The retrieved velocity field clearly follows the expected outflow pattern. While comparisons with tidal current magnitudes predicted by the U.S. National Ocean Service do reveal discrepancies of up to 0.5 m/s, these differences are most likely due to the contribution of ocean surface waves to the overall InSAR velocity measurement. Velocity retrievals for the same area based on the data from different tracks show good consistency. The results constitute the first demonstration of vector retrieval of the surface velocity field with a single-pass InSAR system and confirm the robustness of the dual-beam interferometry principle.**

***Index Terms*—Along-track interferometry, ocean surface currents, synthetic aperture radar (SAR).**

I. Introduction

SINCE its inception [1], [2], along-track synthetic aperture radar interferometry (InSAR) has been a promising and increasingly popular technique for remote sensing of ocean surface phenomena. It can provide detailed maps of oceanic currents and other dynamic surface features. However, in its traditional configuration [1], along-track interferometric SAR (AT-InSAR) measures only one line-of-sight component of the surface velocity vector. Some suggested remedies to allow measurement of full velocity vectors include combining observations from two or more intersecting tracks [3] or inferring the current direction from the bottom topography [4]. Still, these workarounds involve obvious tradeoffs and limitations; therefore, a single-pass *vector* velocity measurement capability would be a very useful and desired development.

Following the idea by Rodriguez *et al.* [5], Frasier and Camps [6] investigated augmenting AT-InSAR to enable such vector velocity mapping. They developed the concept of the dual-beam interferometer (DBI) that was eventually designed and built by the University of Massachusetts (UMass) [7]. DBI combines two AT-InSARs, one squinted 20° forward from broadside, and the other 20° aft. Thus, every scene in the swath is observed from two different directions, which allows reconstruction of the velocity vector.

During 2002–2003, DBI has seen several deployments that addressed mostly engineering and technical issues, with flights in August 2003 producing the first interferograms. The subsequent (and most recent) campaign in March 2004 had science as its primary objective. While attention was focused predominantly on the western Gulf Stream boundary off Cape Canaveral, FL [8], a few overflights of the Florida barrier islands west of Fort Myers were made as well. As before, the instrument was installed on National Oceanic and Atmospheric Administration's (NOAA) WP-3D research aircraft operating out of the NOAA Aircraft Operations Center (AOC) in Tampa, FL. The data were collected and processed as part of a collaboration between UMass and the Naval Research Laboratory (NRL).

The goal of this paper is to present the first examples of single-pass vector velocity retrievals achieved with this new system and to give their qualitative assessment. We concentrate on the observations of currents around barrier islands during high ebb flow, as these data provide a rather comprehensive test of the instrument abilities. Indeed, the outflow patterns in the inlets are sufficiently complex yet intuitively predictable, and independent (though limited) estimates of current velocities in the channels were also available. The high-quality aerial imagery of the site facilitated evaluation of the detected velocity patterns.

Overall, the retrievals produced very reasonable velocity maps, well correlated with the bathymetric features visible in the aerial photos. Vector maps obtained for the same area but from different tracks also show good consistency. Some observed discrepancies in velocity magnitudes are most likely due to contributions from propagating surface waves that are presently not removed by our retrieval algorithms. Other possible sources of error are also identified and estimates are provided.

Manuscript received November 1, 2004; revised February 18, 2005. This work was supported in part by the Naval Research Laboratory under Work Unit 72-8027, in part by the Office of Naval Research under Grant N00014-98-1-0612 to the University of Massachusetts, and in part by a grant of computer time from the DOD High Performance Computing Modernization Program at the Naval Research Laboratory Distributed Center, U.S. Army Engineer Research and Development Center, and the U.S. Army Space and Missile Defense Command Simulation Center.

J. V. Toporkov and M. A. Sletten are with the Remote Sensing Division, Naval Research Laboratory, Washington, DC 20375 USA (e-mail: jakov.toporkov@nrl.navy.mil; mark.sletten@nrl.navy.mil).

D. Perkovic, G. Farquharson, and S. J. Frasier are with the Microwave Remote Sensing Laboratory, University of Massachusetts, Amherst, MA 01003 USA.

Digital Object Identifier 10.1109/TGRS.2005.848603

TABLE I
RADAR PARAMETERS

Parameter	Specification
Center frequency	5.3 GHz
Transmitted signal type	LFM (chirp)
Pulse duration	6.25 μs
Pulse bandwidth	25.0 MHz
Receiver A/D sampling rate	31.25 MHz
Polarization	VV
PRF per channel	1250 Hz
Antenna baseline	1.23 m
Squint angle	20°
Boresight incident angle	70°
Azimuth beamwidth	7°
Elevation beamwidth	31°

TABLE II
TYPICAL OPERATING CONDITIONS

Parameter	Value
Altitude	600 m
Speed	100 m/s
Range within swath (squinted plane)	1.2 - 4.4 km
Incidence angle span	60° - 82°

II. SYSTEM DESIGN AND DATA PROCESSING

A. System Description

The DBI operates at C-band (5.3 GHz) and both transmits and receives using vertical polarization (VV). It emits a 6.25-μs -long chirp signal with a 25-MHz bandwidth that provides a 6-m range resolution. The system has four separate squinted (at $\pm 20°$ with respect to broadside) antennas that form fore- and aft-looking interferometric pairs. The physical baseline in each pair is 1.23 m, with the fore-looking antennas located under their aft-looking counterparts. Only the fore-located antenna in each pair transmits. The antennas are pointed in a 70° incident angle in their squinted planes and have broad elevation (31°) and narrow azimuth (7°) patterns. The received signal is down-converted, sampled at a 31.25-MHz rate and recorded on the hard drives that can store up to 3.5 hours of data. The detailed system description can be found in [7] and [9]; Table I provides a summary of the key parameters.

The instrument is designed to fit in a pod (approximately 2.5 m long and 0.7 m in diameter) that can be attached to various types of aircraft. Currently, the WP-3D aircraft is the preferred platform with the pod being installed on the pylon under its left wing [7], [9]. To date, the instrument has operated at an altitude of 600 m and a ground speed of 100 m/s (cf. Table II). The covered range in the squinted plane is approximately 1.2–4.4 km. The incidence angles in the squinted plane vary from 60° to 82°, which approaches the low-grazing regime. A comprehensive theoretical understanding of the scattering mechanisms in this regime is yet to be developed [10]; hence, extra caution may be warranted in interpreting the data at far ranges. Since for an airborne InSAR the platform motions are usually an issue, DBI has an integrated inertial navigation system/global positioning system (INS/GPS) [11] attached to its frame. This system has differential GPS (DGPS) capability and provides 10-Hz attitude/position data that are used for motion compensation during the processing stages.

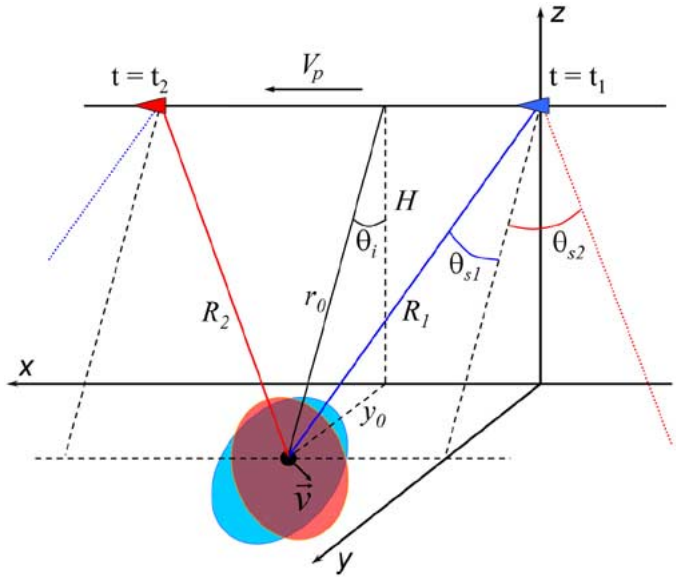

Fig. 1. Instrument observation geometry.

B. SAR Processing

The system geometry is outlined in Fig. 1. During the flight, DBI first observes a scene with the fore-looking AT-InSAR, and then, about 15–20 s later, with its aft-looking counterpart. Complex images for each of four channels (two fore-looking and two aft-looking) are synthesized using the chirp scaling method [12]. No range scaling is used, so the processor places a stationary target on the image at its broadside range r_0 (cf. Fig. 1). The processed data segments are usually about 100 s long.

The motion compensation algorithm uses a flat-Earth assumption and adjusts the data in all four channels to a common single track (the best straight fit to the horizontal trajectory of the INS/GPS device coordinate center), which includes shifts in azimuth to account for the time lag between the fore and rear antennas. This procedure accomplishes several goals. Besides improving the quality of the magnitude images, it removes motion-induced errors from the interferograms and assures that fore-looking and aft-looking images are coregistered (at least for stationary targets).

In flight, the actual squint angles, defined with respect to the track (Fig. 1), are likely to differ from their 20° design values. The causes include variations in aircraft attitude, as well as possible misalignment of the DBI and the airplane axes. For processing purposes, constant squint angles are initially inferred from the averaged navigation data and then refined by estimating Doppler centroid frequencies f_c at midrange, with the relationship being (cf. Fig. 1)

$$f_c = \frac{2V_p}{\lambda} \sin \theta_s. \tag{1}$$

In (1), V_p is the platform velocity, and λ is the electromagnetic wavelength; fore-looking and aft-looking squint angles θ_s are, respectively, assumed to be positive and negative. The effective integration time is specified by applying a filter in the azimuth spectral domain and currently is chosen to be around 1.5 s at midrange—about half of what the 7° antenna pattern would

allow. If the aircraft attitude (mainly heading) fluctuates significantly during the run, there may be times when there are no spectral components near the selected Doppler centroid, which would result in low signal-to-noise ratios (SNRs) in corresponding parts of the image. So far this has not been a problem, and remedies such as processing shorter data segments or using larger integration times are available if this issue arises in the future.

The interferograms Φ_j for fore $(j = 1)$ and aft $(j = 2)$ *squints* are calculated from the corresponding coregistered complex image pairs as

$$\Phi_j(x,r) = \arg\left(\left\langle i_{Fj}(x,r) i^*_{Aj}(x,r)\right\rangle\right), \qquad j = 1,2 \quad (2)$$

where the subscripts "F" and "A" refer to a fore- and aft-*located* antennas constituting each interferometer. The average in (2) is obtained by multilook processing ("coarse-graining") in azimuth to match the 6-m range resolution. With the estimated azimuth resolution of 0.6 m at midrange, this procedure makes use of approximately ten looks. With further reduction in resolution, more robust averages can be obtained if necessary. By the DBI design [6], there should be no phase wrapping for the expected surface velocities of up to approximately 3 m/s. Thus far, we have not encountered a situation when this limit was exceeded and phase unwrapping was necessary.

C. Retrieval of Surface Velocity Vectors

With the knowledge of phase maps Φ_1 and Φ_2 from forward and aft looks, the velocity retrieval proceeds as described in [6]. First, the interferometric phases are related to radial velocities u_j $(j = 1, 2)$ observed at two given squints as

$$u_j = \frac{\Phi_j}{4\pi}\frac{\lambda}{B_e} V_p. \quad (3)$$

Because only one antenna in each pair is transmitting, the effective baseline B_e in (3) equals half the physical along-track antenna separation.

Assuming that surface velocities are confined to horizontal plane, their components are computed as (cf. Fig. 1)

$$v_x = \frac{u_1 \cos\theta_{s2} - u_2 \cos\theta_{s1}}{\sin(\theta_{s1} - \theta_{s2})}$$
$$v_y = \frac{u_2 \sin\theta_{s1} - u_1 \sin\theta_{s2}}{\sin(\theta_{s1} - \theta_{s2})\sin\theta_i}. \quad (4)$$

As stated previously, the aft-looking squint angle is assumed to be negative. The above two equations extend the result (11) in [6] to the case of two arbitrary squints. Note also that [6] uses different angle definitions.

In what follows, we present the retrieved velocity fields (4) sometimes calling them "currents." It should be noted, however, that for sea surface observations, the measured interferometric phases (2) and derived velocities (4) contain contributions from both ambient currents and propagating surface waves [3], [13]. The latter component can be appreciable and, ideally, should be taken out. Accurate removal is an interesting and challenging task by itself (e.g., [14]) and requires, among other things, good knowledge of the surface and wind conditions in the area (if the DBI was *calibrated*, it could supply some of these data by doubling as a dual-beam wind scatterometer). While *no such correction is attempted here*, we will provide an estimate of the surface roughness contribution and its impact.

III. Results and Discussion

A. Overview

The processing techniques described above were applied to the DBI data gathered over the barrier islands west of Fort Myers, FL on March 13, 2004. The flight was scheduled around the expected time of maximum ebb current, based on daily predictions by the NOAA's National Ocean Service (NOS).[1] Flight tracks consisted of several northbound and southbound passes parallel to the island chain; a few perpendicular, east–west passes over a couple of selected inlets were made as well.

Part of that study area is shown in Fig. 2. The land mass seen on the right is Pine Island which encloses the sound from the east. The two inlets in the island chain on the left, Captiva Pass and Redfish Pass, will be the focus of our analysis. The body of water to the left is the Gulf of Mexico. Fig. 2 also includes an aerial photograph of the site.[2] The image is dated February 1, 2003 and reveals some bathymetric information. Since no detailed bathymetry maps are available to us at this time, we rely on this aerial imagery when assessing the retrieved velocity patterns.

As Fig. 2 illustrates, the scene was observed from two opposite parallel tracks. The data segment corresponding to Track 1 began at 22:36:50 EST and lasted 100 s. The data from Track 2 last 104 s and were collected 12.5 min later, starting at 22:49:25 EST. We emphasize that only one track is necessary for DBI measurement of vector velocity field. Unless stipulated otherwise, the data discussed below are from Track 1, with Track 2 used for comparisons and confirmation of the findings.

B. Retrieved Velocities

Fig. 3 displays the coherence map (a) and the interferogram (b) for the aft look at 6-m resolution [for SAR intensity image, cf. Fig. 4(a)]. Changes in phase are clearly visible around the channels. As expected, the coherence stays high over the land with typical values of 0.95 and above. The coherence is lower over the water due to temporal decorrelation and weaker backscatter (lower SNR). The latter effect becomes particularly noticeable at distant ranges. The coherence and phase might also be affected by other factors such as instrumental and processing artifacts, including range sidelobes from bright land. As expected, in the regions with low coherence the phase becomes increasingly noisy. Therefore, for velocity retrieval we will use a boxcar window to get additional 20×20 pixel averaging as described in Section II. However, in the vicinity of the inlets, the SNR and coherence remain strong, which allows mapping the currents there at higher (e.g., 6×6 m) resolution if necessary.

The retrieved vector velocity field is shown in Fig. 4 superimposed on the SAR intensity image (a) and on a color-coded map of the velocity magnitude (b). The velocities in both channels

[1]http://co-ops.nos.noaa.gov/currents04/

[2]Aerial Imagery by GlobeXplorer acquired through the U.S. National Geographic website http://mapmachine/nationalgeographic.com.

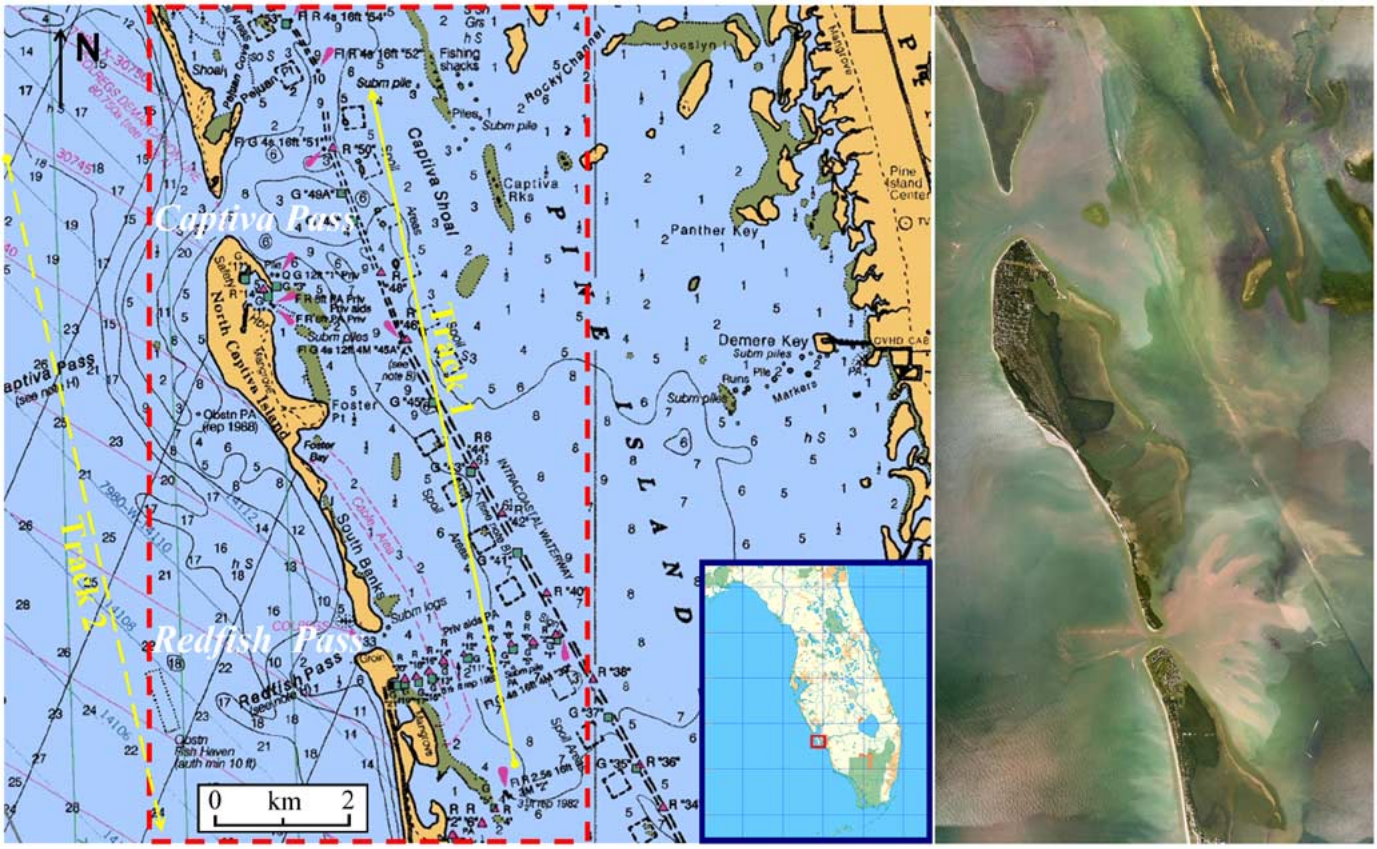

Fig. 2. (Left) Map of the study area and (right) the aerial photograph corresponding to the dashed red box on the map.

clearly show the outflow patterns that one might expect from the aerial imagery in Fig. 2. In particular, the green hue in the sound likely indicates algae growth that would be characteristic of shallower areas with stagnant water. On the contrary, the tan or pink-colored areas around the inlets suggest appreciable currents and bear witness to their erosion effects. From this, we expect that the current influx in the Captiva Pass inlet would be predominantly from northeast and southeast directions, with the approach from due east being obstructed by a protruding shoal. This behavior is indeed observed in Fig. 4. Later in the paper we will analyze the inlet areas (dashed boxes) in more detail.

Some minor anomalies in Fig. 4(b) can also be observed. For example, large velocities detected for a spot east of Captiva Pass (around 2 km ground range and 9 km azimuth) are most likely due to the presence of a moving object (appearing only in fore-looking channels). The sources of relatively large velocities near the shore at 2.8 km ground range and 5.5–6 km azimuth are, as yet, undetermined, and increased velocity values at far range should be treated with suspicion because of low SNR as discussed above.

The only independent velocity estimates available to us for comparison were the NOS predictions of tidal currents. The NOS data indicate that ebb current in Captiva Pass on March 13, 2004 peaked at 22:10:00 EST (i.e., 27 min prior to Track 1 data acquisition) with a value of 0.8 m/s. Our measurements across the Captiva inlet yield absolute velocity values of 1.1–1.2 m/s, and outside the channel the retrieved outflow pattern exhibits varying structure with peak magnitude reaching 1.7 m/s. No NOS data were available for the narrower Redfish Pass where we detect a stronger, more uniform flow of 1.75 m/s. It is not entirely clear to what precise geographical point the NOS prediction refers to, or what spatial averaging is used in their model. All those considerations are important because of the substantial spatial variability of the current being observed. Perhaps high-fidelity hydrological models similar to KUSTWAD described in [15] could provide better comparison if available. Still, a difference on the order of 0.5 m/s is acknowledged. As we show next, a plausible source of this discrepancy is wind-generated surface roughness.

C. Error Analysis

We now consider the factors most likely to affect the accuracy of InSAR current measurements: phase errors due to low coherence and residual motion errors. The bias introduced by the surface waves, while being more of a postprocessing rather than a system problem, is also estimated.

For phase error variance, we use a Cramer–Rao bound [16], [17]

$$\sigma_{\Phi}^2 = \frac{1}{2N_L}\frac{1-\gamma^2}{\gamma^2}. \tag{5}$$

The coherence γ (absolute value of the complex correlation coefficient) is determined from maps similar to one in Fig. 3(a) using additional 20×20 pixel averaging to improve the estimate. The number of looks N_L in this case varies from about 2200 to 7500, depending on range.

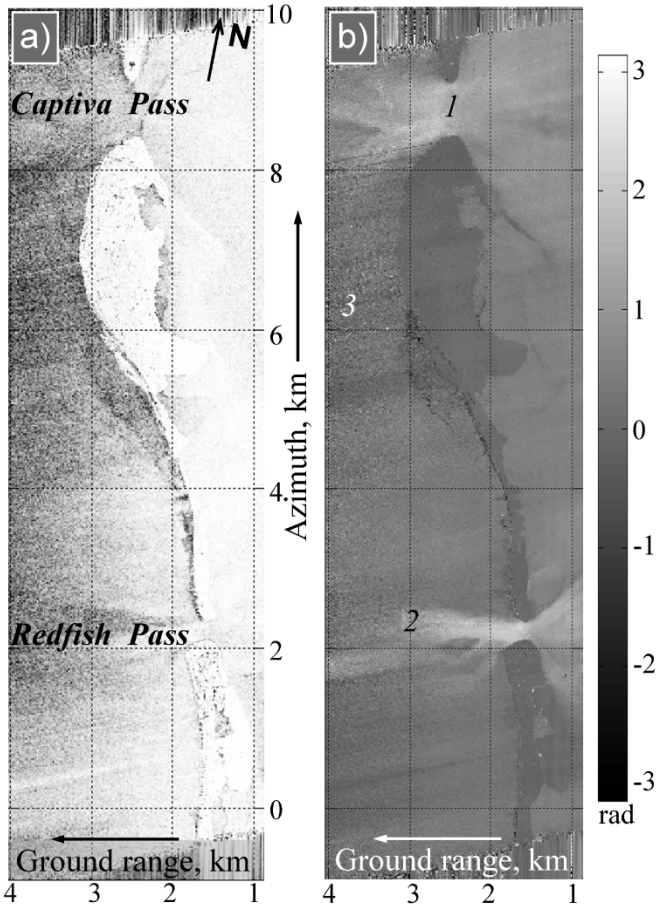

Fig. 3. (a) Coherence map and (b) interferometric phase for the aft look. Numbers in (b) specify locations for which phase errors will be estimated.

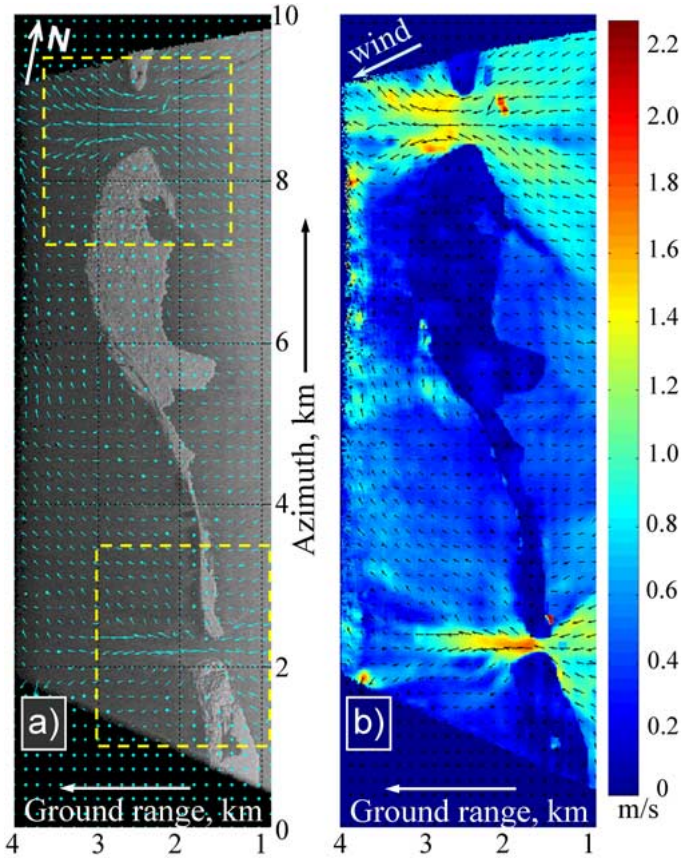

Fig. 4. Retrieved vector velocity field superimposed on (a) SAR intensity image and (b) on color-coded map of velocity magnitudes. Yellow dashed boxes indicate areas to be analyzed in detail.

Variances for the velocity component estimates can be derived from (3) and (4) assuming that phase noise in the aft- and fore-looking interferograms is uncorrelated (cf. also [6])

$$\sigma_{vx}^2 = \left(\frac{\lambda V_p}{4\pi B_e}\right)^2 \frac{\sigma_{\Phi 1}^2 \cos^2\theta_{s2} + \sigma_{\Phi 2}^2 \cos^2\theta_{s1}}{\sin^2(\theta_{s1}-\theta_{s2})}$$
$$\sigma_{vy}^2 = \left(\frac{\lambda V_p}{4\pi B_e}\right)^2 \frac{\sigma_{\Phi 1}^2 \sin^2\theta_{s2} + \sigma_{\Phi 2}^2 \sin^2\theta_{s1}}{\sin^2(\theta_{s1}-\theta_{s2})\sin^2\theta_i}. \quad (6)$$

The overall accuracy of the retrieved velocity vector due to phase errors is

$$\sigma_{\vec{v}}^2 = \sigma_{vx}^2 + \sigma_{vy}^2. \quad (7)$$

Error in the velocity *magnitude* v may also be of interest. For $\sigma_{\vec{v}}/v < 1$, it can be estimated as

$$\sigma_v^2 = \frac{v_x^2\sigma_{vx}^2 + v_y^2\sigma_{vy}^2 + 2v_x v_y \sigma_{vx}\sigma_{vy}\rho}{v_x^2 + v_y^2} \quad (8)$$

TABLE III
ERRORS DUE TO INTERFEROMETRIC DECORRELATION

Location (Fig. 3b)	Coherence		σ_Φ, rad		v_x, m/s	v_y, m/s	v, m/s	$\sigma_{\vec{v}}$, m/s	σ_v, m/s
	Fore	Aft	Fore	Aft					
1	0.83	0.67	0.008	0.014	-0.01	1.15	1.15	0.02	0.01
2	0.41	0.60	0.029	0.018	-0.15	0.86	0.87	0.04	0.01
3	0.08	0.41	0.182	0.032	0.113	0.23	0.26	0.22	0.14

where ρ is the correlation coefficient between the errors in the x- and y- velocity components, shown in (9) at the bottom of the page. Table III summarizes phase and velocity errors calculated according to (5)–(9) for three locations labeled in Fig. 3(b). The accuracy of vector velocity estimate $\sigma_{\vec{v}}$ at locations 1 and 2 is better than 4 cm/s, and the impact on the velocity magnitude (given by σ_v) is even smaller. The worst accuracy is achieved for location 3, due to very low coherence in the fore-looking channels. It is obvious that the velocity estimate of 0.26 m/s there is

$$\rho = -\frac{\sigma_{\Phi 1}^2 \sin(2\theta_{s2}) + \sigma_{\Phi 2}^2 \sin(2\theta_{s1})}{2\sqrt{\left(\sigma_{\Phi 1}^2 \cos^2\theta_{s2} + \sigma_{\Phi 2}^2 \cos^2\theta_{s1}\right)\left(\sigma_{\Phi 1}^2 \sin^2\theta_{s2} + \sigma_{\Phi 2}^2 \sin^2\theta_{s1}\right)}} \quad (9)$$

dominated by errors ($\sigma_{\vec{v}} = 0.22$ m/s), so strictly speaking (8) is not applicable and apparently gives an underestimated value.

After SAR processing with motion compensation, slow phase undulations in azimuth direction are still noticeable. They can be spotted in Fig. 3(b) as tilted bands extending in a squinted range direction. A similar effect was reported by Prats and Mallorqui [18] and was linked to insufficient precision of INS/GPS systems. We estimate these residual phase undulations to be on average 0.1 rad in both the fore- and aft-looking channels. Their period varies but generally stays under 5 s. As observations of a particular scene through the fore- and aft-squinted beams are separated in time by 10 s or more, unintended platform motion at a given instant in time affects regions in the two interferograms that are widely separated in space. Therefore, we will assume that for a given image pixel the two sources of phase noise are uncorrelated. Repeating calculations in (6) with $\sigma_{\Phi 1} = \sigma_{\Phi 2} = 0.1$ rad, we find that residual motion errors introduce vector velocity inaccuracies $\sigma_{\vec{v}}$ of 0.17 m/s. As this error does not depend on local image properties like the coherence and varies only mildly with the observation geometry, it is characteristic of the whole scene. We can verify this estimate by looking at the land areas in Fig. 4(b). Ideally, the phase over land should be zero, yet the retrieval yields some nonzero velocities, and the residual motion errors are most likely the cause. These observed spurious velocities are indeed mostly of the order of 0.1–0.2 m/s. The effect of motion errors on the magnitudes of retrieved currents can be gauged using (8). For Captiva pass (location 1, cf. Fig. 3) such an error corresponds to 0.06 m/s. This is still well below the discrepancy with the NOS data discussed earlier.

To assess the impact of surface waves on our measurements, we need to estimate the mean frequency f_D of the Doppler spectrum that such waves would produce without any current [13]. It is this frequency that introduces an additional phase shift of $-2\pi f_D(B_e/V_p)$ to the interferogram and gets interpreted as a radial velocity [cf. (3)]

$$u_D = -\frac{\lambda f_D}{2}. \tag{10}$$

As f_D depends on the sea state, knowledge of surface conditions is certainly required. During the hour that these data were collected, the closest NOS station at Fort Myers (30 km inland from the islands) reported the easterly wind (98° from true north) with average speed of 3 m/s and gusts of up to 5 m/s. A 22:40 EST report from the local meteorological station on Gasparilla Island (40 km north) indicated a northeast wind (53° from true north) with average speed of 5 m/s and 6-m/s gusts. We believe that the Gasparilla Island station report is more representative of the coastal conditions; also the wind streaks observed in some SAR imagery appear to be in better agreement with the wind direction stated there.

Romeiser and Thompson [14] proposed an efficient method that evaluates the roughness-induced f_D based on a two-scale scattering model using the ocean surface wave spectrum as an input. Long gravity waves with wavelengths exceeding the resolution element may require separate, deterministic treatment; however, no such waves or their phase signatures are visible in the 6 × 6 m-resolution imagery [cf. Figs. 4(a) and 3(b)], and additional smoothing with the 20-by-20 pixel window used in the retrievals further alleviates any such concerns. Although the DBI incidence angles are outside the stated region of validity of the Romeiser–Thompson model (30° to 60°), earlier two-dimensional (2-D) comparisons with direct numerical simulations of the surface backscatter [19] indicate that reasonable predictions still can be obtained for larger angles. For a rough estimate, we will use the reduced 2-D model implementation (with only one horizontal coordinate) from that study. While the 2-D case corresponds to rather special circumstances in which the radar looks either up- or downwind, we observe that such a situation is almost realized for the aft-looking antenna [cf. wind direction in Fig. 4(b)]. With a 5-m/s Pierson–Moskowitz surface spectrum (e.g., see [20]), we estimate f_D in the aft look to be about −13 Hz for the whole range of our incidence angles. Unfortunately, 2-D analyses cannot provide answers for cases of considerable cross-wind looks that occur for the fore beams. Yet we note that in the cross-wind case a radar observes both receding and advancing waves, resulting in contributions at both positive and negative Doppler frequencies [13], [14], [21]. The mean frequency f_D therefore should be smaller than for the up- or downwind look. To proceed with our estimate, we set f_D for the fore look to half the aft look value, i.e., −6.5 Hz. Calculations using (10) and (4) show that wind-generated surface roughness contributes −0.24 m/s in the x direction, and 0.33 m/s in the y. Removing these components would cause the velocity magnitude at location 1 (in Captiva Pass) to drop from 1.15 to 0.85 m/s, a value that is much closer to the NOS predictions. The adjusted velocity vector will be rotated clockwise (toward north) by 16°. We can repeat these calculations for the region about 200 m westward, just outside Captiva pass, where we observed even higher currents. The velocity magnitude there drops from 1.3 to 0.98 m/s, with the direction adjusted by 13.5° clockwise. This simple estimate shows that surface waves are indeed an important factor and that accounting for their effects does bring the retrieved velocities closer to the NOS current predictions. We also note that our vector velocity maps, though biased by surface waves, should still provide reasonable estimates of the directions and patterns of the dominant currents. In comparison, phase noise and residual motion errors appear to have fairly limited impact on the accuracy of our results.

D. Detailed Examination of Inlet Patterns and Comparison With Track 2 Data

With better understanding of the accuracy of our retrievals, we now take a closer look at velocity fields in the two inlets. As before, we use the aerial imagery to confirm and explain various features observed in the retrieved patterns.

We first turn to Redfish Pass for which our retrievals in Fig. 5(a) and (b) show a very strong and narrow outflow current. The photograph in Fig. 5(c) reveals an expanding channel-like underwater feature that is well correlated with the velocity pattern. The upper and lower edges are probably sandbars that come very close to the surface, as evidenced by breaking waves in the photo at location A as well as in other places along those boundaries. Such bottom topography should indeed confine and direct the outflow current, just as our data show.

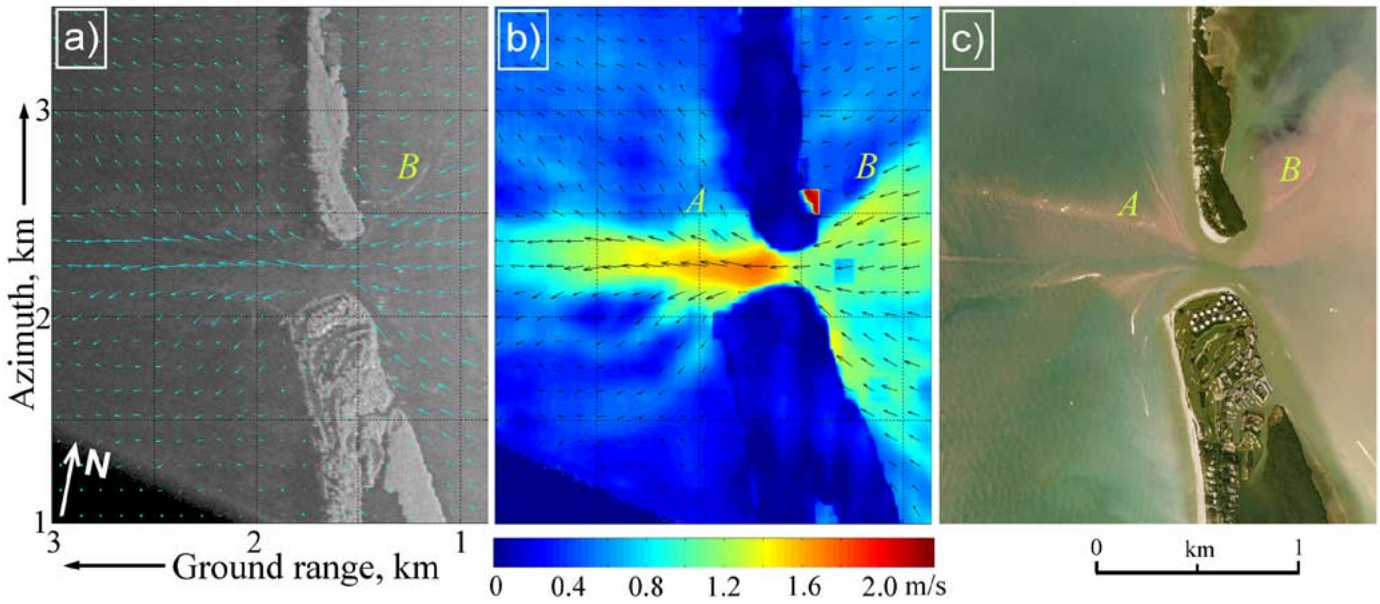

Fig. 5. Detailed look at Redfish Pass [bottom box in Fig. 4(a)]. (a) SAR intensity image and (b) color-coded map of velocity magnitudes with velocity vectors superimposed. (c) Aerial photography image of the same area. Capital letters indicate features identifiable in more than one image.

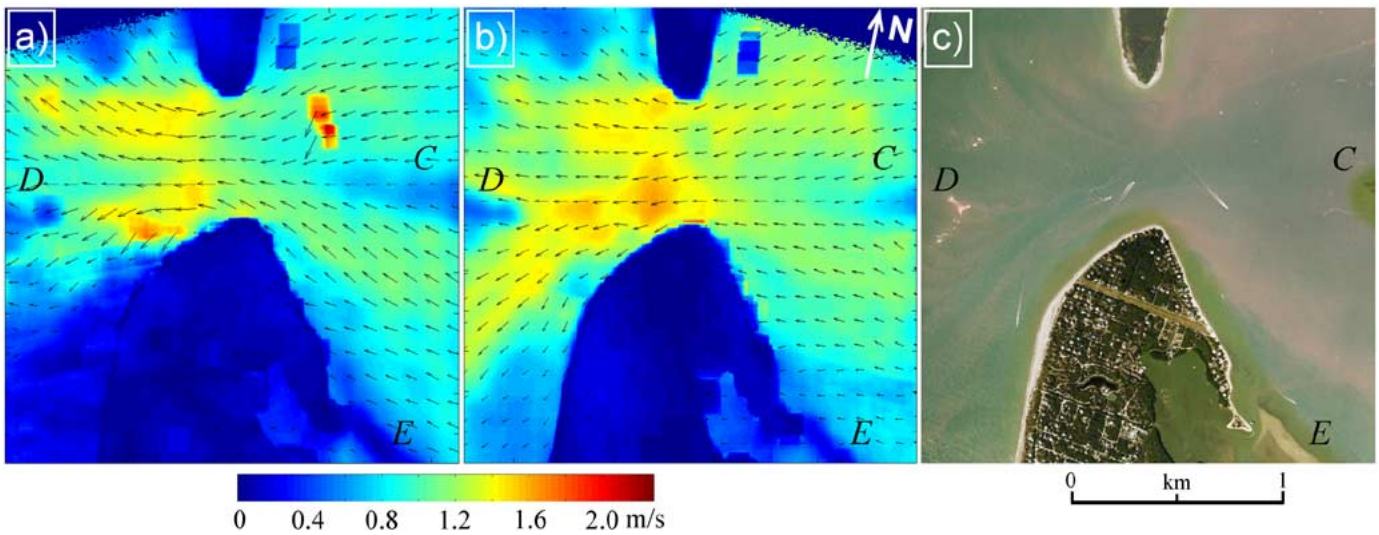

Fig. 6. Detailed look at Captiva Pass [top box in Fig. 4(a)]. (a) Color-coded velocity magnitudes and directional map from Track 1 (scene viewed from the right). (b) Same plot with data from Track 2 (scene viewed from the left). (c) Aerial photography image of the area. Capital letters indicate some of the features identifiable in all images.

Another observation that Fig. 5(b) offers is a curious boundary B on the inner northern side of the inlet above which the velocity sharply drops. This is in contrast with the southern part of the inflow pattern that extends all the way to the shoreline. The photo in Fig. 5(c) does show a bright curve at this location. Moreover, the same curved line is visible in the SAR intensity image [Fig. 5(a)] as well. We speculate that this is another sandbar or a man-made structure, such as a jetty, that obstructs the inflow current keeping it away from the shore.

Finally, we compare velocity patterns obtained from different tracks using Captiva Pass as an example. Fig. 6(a) offers a closer look at the flow pattern that we already saw as part of Fig. 4 (upper dashed box there). The velocity map for the same area was also retrieved using data from Track 2 and is shown in Fig. 6(b). Again, Fig. 6(c) offers an aerial photograph of the scene.

The difference to notice in the two images is that the velocity magnitudes in Fig. 6(b) have increased across the whole scene by about 0.2 m/s. As it was already past the time of maximum ebb current, and the data in Fig. 6(b) trail Fig. 6(a) by 11 min, stronger current is an unlikely explanation. Based on our discussion of error sources, it is reasonable to conclude that changes in the surface roughness contribution are the most probable cause. During the time between the tracks, the wind might have increased and stronger waves developed; change in observation direction coupled with upwind/downwind asymmetries in wave shapes and scattering properties could have also played a role. This yet again underscores the need for proper removal of wave

contributions backed by good knowledge of local sea surface conditions.

Another apparent difference is spotted in the lower left corners of the two velocity maps. While Fig. 6(b) shows a steady southwest flow in that area, no similar persistent pattern is visible in Fig. 6(a). We suspect that this "missing current" in the part of Track 1 data is due to contamination of phase by strong range sidelobes cast by bright land. During Track 2 acquisition, the scene was viewed from the opposite direction, which precluded the problem.

Aside from these discrepancies, the two patterns are rather similar, and many common features can be identified. For example, a green spot (labeled C) on the aerial image in Fig. 6(c) is most likely a detached part of the larger Captiva Shoal that lies further to the east (cf. also Fig. 2). This shoal obstructs the westward current, as evident in both Fig. 6(a) and (b). A similar effect is observed at location D where vigorous wave breaking visible in the aerial image indicates another shoal. Finally, a sandbar or a jetty E [traceable in the SAR intensity image in Fig. 4(a)] prevents strong current from approaching the island's inner shore.

IV. Conclusion

Dual-beam along-track SAR interferometry offers the unique capability of obtaining detailed maps of full surface velocity vectors in a single aircraft pass. Such vector velocity information is of value in many areas, oceanographic studies and coastal engineering being the most obvious examples. DBI can routinely collect these data for extended regions and update them as needed.

In this paper, we presented the first vector velocity measurements produced with this unique newly developed UMass instrument. The analysis focused on tidal currents in the coastal area, and the DBI yielded reasonable and realistic outflow signatures. The observed flow patterns correlate well with bathymetric features inferred from aerial photography, and measurements obtained from different flight tracks generally show consistency.

Ebb current predictions published by the National Ocean Service were used for quantitative comparisons and revealed a discrepancy about 0.5 m/s with our data. The error analysis showed that the likely cause is a Doppler contribution from the surface waves, a known bias in AT-InSAR current estimates. The residual motion errors are the next significant factor affecting the accuracy. Phase noise due to decorrelation might present a problem at far range where SNR becomes low, but can be suppressed by averaging a large number of looks while still maintaining an acceptable level of detail.

All these issues are recognized and will be addressed in the future. Still, the results in this paper show that the DBI produces reasonable and quite consistent single-pass estimates of full surface velocity vectors, as it detects and maps complex current patterns. These first results demonstrate the robustness of the dual-beam interferometry concept and serve as sound testimony to the new system's capabilities and promise.

Acknowledgment

The authors would like to thank the NOAA Aircraft Operations Center, Tampa, FL, for their generous logistical and technical support. The comments by anonymous reviewers are also gratefully acknowledged.

References

[1] R. M. Goldstein and H. A. Zebker, "Interferometric radar measurements of ocean surface currents," *Nature*, vol. 328, pp. 707–709, 1987.

[2] R. M. Goldstein, T. P. Barnett, and H. A. Zebker, "Remote sensing of ocean currents," *Science*, vol. 246, pp. 1282–1285, 1989.

[3] H. C. Graber, D. R. Thompson, and R. E. Carande, "Ocean surface features and currents measured with synthetic aperture radar interferometry and HF radar," *J. Geophys. Res.*, vol. 101, no. C11, pp. 25 813–25832, 1996.

[4] R. Romeiser, H. Runge, H. Breit, M. Eineder, and P. Flament, "Toward an operational spaceborne system for high-resolution current measurements in coastal areas," in *Proc. IEEE OCEANS Conf.*, San Diego, CA, 2003, pp. 1524–1530.

[5] E. Rodriguez, D. Imel, and B. Houshmand, "Two-dimensional surface currents using vector along-track interferometry," in *Proc. PIERS'95 Conf.*, Seattle, WA, 1995, p. 763.

[6] S. J. Frasier and A. J. Camps, "Dual-beam interferometry for ocean surface current vector mapping," *IEEE Trans. Geosci. Remote Sensing*, vol. 39, no. 2, pp. 401–414, Feb. 2001.

[7] G. Farquharson, W. N. Junek, A. Ramanathan, S. J. Frasier, R. Tessier, D. J. McLaughlin, M. A. Sletten, and J. V. Toporkov, "A pod-based dual-beam SAR," *IEEE Geosci. Remote Sens. Lett.*, vol. 1, no. 2, pp. 62–65, Apr. 2004.

[8] D. Perkovic, J. V. Toporkov, M. A. Sletten, G. Farquharson, S. J. Frasier, and G. O. Marmorino, "Gulf stream surface velocity measurements obtained with the UMass dual beam interferometer in conjunction with NRL infrared camera," in *Proc. IGARSS*, Anchorage, AK, Sep. 2004, pp. 3325–3328.

[9] D. Perkovic, S. J. Frasier, R. Tessier, M. A. Sletten, and J. V. Toporkov, "An airborne pod-mounted dual beam interferometer," in *Proc. IEEE Aerospace Conf.*, Big Sky, MT, Mar. 2005, pp. 1–10.

[10] G. S. Brown, "Guest editorial—Special issue on low-grazing-angle backscatter from rough surfaces," *IEEE Trans. Antennas Propagat.*, vol. 46, no. 1, pp. 1–2, Jan. 1998.

[11] M. K. Martin and B. C. Detterich, "C-MIGITS II design and performance," in *Proc. Satellite Division of the Institute of Navigation 10th Int. Technical Meeting: ION GPS-97*, Kansas City, MO, Sep. 1997, pp. 95–102.

[12] A. Moreira and Y. Huang, "Airborne SAR processing of highly squinted data using a chirp scaling approach with integrated motion compensation," *IEEE Trans. Geosci. Remote Sens.*, vol. 32, no. 5, pp. 1029–1040, Sep. 1994.

[13] D. R. Thompson and J. R. Jensen, "Synthetic aperture radar interferometry applied to ship-generated internal waves in the 1989 Loch Linnhe experiment," *J. Geophys. Res.*, vol. 98, no. C6, pp. 10 259–10 269, 1993.

[14] R. Romeiser and D. R. Thompson, "Numerical study on the along-track interferometric radar imaging mechanism of oceanic surface current," *IEEE Trans. Geosci. Remote Sensing*, vol. 38, no. 1, pp. 446–458, Jan. 2000.

[15] R. Romeiser, H. Breit, M. Eineder, H. Runge, P. Flament, K. de Jong, and J. Vogelzang, "Validation of SRTM-derived surface currents off the Dutch coast by numerical circulation model results," in *Proc. IGARSS*, Toulouse, France, Jul. 2003, pp. 3085–3087.

[16] E. Rodrigues and J. M. Martin, "Theory and design of interferometric synthetic aperture radars," *Proc. Inst. Elect. Eng. F*, vol. 139, no. 2, pp. 147–159, 1992.

[17] P. A. Rosen, S. Hensley, I. R. Joughin, F. K. Li, S. N. Madsen, E. Rodriguez, and R. M. Goldstein, "Synthetic aperture radar interferometry," *Proc. IEEE*, vol. 88, no. 3, pp. 333–382, Mar. 2000.

[18] P. Prats and J. J. Mallorqui, "Estimation of azimuth phase undulations with multisquint processing in airborne interferometric SAR images," *IEEE Trans. Geosci. Remote Sens.*, vol. 41, no. 6, pp. 1530–1533, Jun. 2003.

[19] J. V. Toporkov, M. A. Sletten, and G. S. Brown, "Numerical scattering simulations from time-evolving ocean-like surfaces at L- and X-band: Doppler analysis and comparisons with a composite surface analytical model," in *Proc. General Assembly of the International Union of Radio Science (URSI)*, Maastricht, The Netherlands, Aug. 2002.

[20] J. V. Toporkov and G. S. Brown, "Numerical simulations of scattering from time-varying, randomly rough surfaces," *IEEE Trans. Geosci. Remote Sens.*, vol. 38, no. 4, pp. 1616–1625, Jul. 2000.

[21] D. R. Thompson, "Doppler spectra from the ocean surface with a time-dependent composite model," in *Radar Scattering From Modulated Wind Waves*, G. J. Komen and W. A. Oost, Eds. Norwell, MA: Kluwer, 1989, pp. 27–40.

Jakov V. Toporkov (S'95–A'98–M'03–SM'04) received the M.S. degree (with distinction) in electronics engineering from the Moscow Institute of Physics and Technology, Moscow, Russia, and the M.S. and Ph.D. degrees in physics from the Virginia Polytechnic Institute and State University (Virginia Tech), Blacksburg, in 1989, 1996, and 1998, respectively.

From 1989 to 1993, he was employed in Russia as an Engineer-Researcher and was involved in the design of synthetic aperture radars. In 1998–1999, he held a postdoctoral appointment at the Bradley Department of Electrical and Computer Engineering, Virginia Tech, where he worked on the numerical simulation studies of scattering from randomly rough ocean-like surfaces. In 1999, he joined SFA, Inc., Largo, MD and was stationed at the Naval Research Laboratory, Washington, DC. There he was engaged in development of image processing capabilities for ultrawideband light airborne SAR system and in studies of scattering from ocean surface at low grazing angles. Since 2002, he has been a Research Physicist at the Naval Research Laboratory. His present research interests include physics of wave scattering by sea surface and SAR remote sensing of the ocean.

Dr. Toporkov is a member of Commission F of the U.S. National Committee of the International Union of Radio Science (USNC-URSI). In 1999, together with his coauthors R. Marchand and G. Brown, he was a recipient of the IEEE Antennas and Propagation Society Schelkunoff Best Paper Award.

Dragana Perkovic (S'00) received the B.S. degree in electrical engineering from the University of Malta, Msida, Malta, in 2002 with a major in telecommunications and computing. She is currently pursuing the Ph.D. degree at the University of Massachusetts, Amherst (UMass-Amherst).

She is a Research Assistant in the Microwave Remote Sensing Laboratory, UMass-Amherst. Her research focuses on instrumentation, signal processing, and applications in radar oceanography.

Gordon Farquharson (S'01–M'05) received the B.S. (Eng.) and M.S. (Eng.) degrees from the University of Cape Town, Cape Town, South Africa, and the Ph.D. degree in electrical engineering from the University of Massachusetts, Amherst, in 1996, 1999, and 2005, respectively. His dissertation research focused on the interpretation of microwave imaging radar measurements of nearshore ocean processes.

In 2004, he joined the National Center for Atmospheric Research, Boulder, CO, where he develops and conducts research into microwave remote sensing radars for atmospheric research.

Mark A. Sletten (S'87–M'91–SM'04) received the B.S., M.S., and Ph.D. degrees in electrical engineering from the University of Wisconsin, Madison in 1984, 1987, and 1991, respectively.

From 1985 to 1987, he was a Research Assistant and ECE Department Fellow at the Wisconsin Center for Applied Microelectronics. As a doctoral student under the Rockwell International Doctoral Fellowship Program, his research included experimental and theoretical investigations of polarization-altering guided wave optical devices. Since joining the Naval Research Laboratory, Washington, DC, in 1991, he has been engaged in radar-based ocean remote sensing research. This work includes the development of ultrawideband polarimetric systems for determining the fundamental physics underlying low-grazing-angle radar sea scatter, and the development and use of airborne radar systems (both real and synthetic aperture) for remote sensing of the coastal ocean. Past work has included a real-aperture radar study of the Chesapeake Bay outflow plume, and the development of a lightweight, multiband, interferometric SAR for use on a light aircraft. More recently, he has conducted several field experiments that investigated the use of interferometric SAR systems for measuring ocean surface currents and mapping the space–time evolution of submesoscale oceanic eddies.

Stephen J. Frasier (S'93–M'95–SM'03) received the B.E.E. degree from the University of Delaware, Newark, and the Ph.D. degree from the University of Massachusetts, Amherst (UMass–Amherst), in 1987 and 1994, respectively.

From 1987 to 1990, he was with SciTec, Inc., a subsidiary of TRW, where he worked on signal processing and analysis of EM and IR signatures of rocket plumes, evaluation of laser detection systems, and development of data acquisition systems for airborne IR sensors. In August 1990, he joined the Microwave Remote Sensing Laboratory, UMass–Amherst. His graduate work involved the development and application of a phased-array imaging radar for air–sea interaction research. From 1994 to 1997, he was employed by UMass–Amherst as a Research Engineer and Senior Research Fellow. In 1997, he joined the faculty of the Electrical and Computer Engineering Department as an Assistant Professor. He is currently an Associate Professor and Director of the Microwave Remote Sensing Laboratory. His research interests include microwave imaging and interferometry, radio oceanography, and remote sensing of the atmospheric boundary layer. He is an Associate Editor of the journal *Radio Science*.

Dr. Frasier has served as Chair of the Springfield (MA) chapter of the IEEE Geoscience and Remote Sensing Society. He is a member of the American Meteorological Society and the American Geophysical Union.